Effect of Si(IV) substitution on electrochemical, magnetic and spectroscopic performance of nanosized $LiMn_{2-x}Si_xO_4$

Amaia Iturrondobeitia,[a] Aintzane Goñi,[a] Luis Lezama,[a] Chunjoong Kim,[b] Marca Doeff,[b] Jordi Cabana[b] and Teófilo Rojo*[ac]

Received (in XXX, XXX) Xth XXXXXXXXX 20XX, Accepted Xth XXXXXXXXX 20XX
DOI: 10.1039/b000000x

We report a simple and cheap process for the synthesis of Si substituted $LiMn_2O_4$. The resulting materials are composed of partially sintered particles of 80 nm average size, corresponding to single crystalline phases with cubic spinel structures. The substitution of Mn(IV) by Si(IV) in the crystal framework changed the cell parameter and volume, and was confirmed by the evolution observed in the XPS and ESR measurements. A complete magnetic study was carried out. Due to the in-built magnetic frustration within the spinel structure and the competition between different exchange pathways, the insertion of different quantities of Si(IV) causes significant differences in the properties. The electrochemical study revealed that introducing a small amount of Si (IV) enhances the electrochemical performance of the spinel. The highest specific capacity and rate discharge capability were obtained for $LiMn_{1.95}Si_{0.05}O_4$, while insertion of a higher amount of the tetravalent dopant caused deterioration of the electrochemical behavior.

Introduction

The lithium manganese oxide spinel, $LiMn_2O_4$, is currently one of the most popular cathode materials for Li-ion batteries due to its low cost, non-toxicity, the abundance of manganese resources, its facile production and excellent safety [1,2.] $LiMn_2O_4$ crystallizes in the Fd-3m space group with Mn (III) and Mn (IV) ions residing in the 16d octahedral sites and Li ions occupying 8a tetrahedral sites located in the tridimensional channels of the framework. Although $LiMn_2O_4$ and its variants have many advantages, they still suffer from capacity fading during cycling. It is known that the capacity fading is caused by several factors such as manganese dissolution into the electrolyte [3], Jahn-Teller distortion due to Mn (III) ions [4] and change in crystal lattice arrangement with cycling [5]. In order to overcome the capacity fade caused by the Jahn-Teller distortion, many authors have suggested substituting some of the manganese with trivalent or divalent cations in order to reduce the resultant Mn (III) content [6,7]. There are number of reports on the influence of substitutions with many 3d transition and non transition metal ions [8-10]. However, the reduction of the amount of the active Mn (III) species decreases the maximum value of the capacity that can be reached in the 3.5-4.2 V range. Thus, it may be expected that replacing part of the manganese with a tetravalent dopant, suchs as Si (IV), could increase the stability of the spinel structure without decreasing the amount of Mn (III) active species, resulting in improved cycling. Previous studies of our group confirmed that inserting a small amount of Si (IV) in the structure resulted in more larger and more regular MnO_6 octahedra, which can more readily accomodate the Mn(III)-

Mn(IV) redox change [11].

Another important factor to be considered is the influence that particle size and morphology have on the electrochemical properties. In some cases, cathode material compounds prepared in nanostructured form exhibit enhanced electrochemical properties [12,13]. Here, we have employed a freeze-drying synthesis procedure for Si substituted $LiMn_2O_4$, which, as well as being a cheap and easy method, can be implemented as part of an industrial process. This synthesis method has been already proved in our group to be useful to obtain nanosized cathodic materials with exceptional electrochemical performance [14,15].

We report the magnetic, spectroscopic and electrochemical characterization of the synthesized samples, establishing correlations between the composition, morphology and electrochemical performance.

Experimental

Sample Preparation

$LiMn_{2-x}Si_xO_4$ ($0 \leq x \leq 0.2$) samples were synthesized by a freeze-drying method. First $C_6H_8O_7 \cdot H_2O$, $Mn(C_2H_3O_2)_3 \cdot 2H_2O$, $Si(CH_3COO)_4$ and $LiOH \cdot H_2O$ were dissolved in 25 ml of H_2O with different molar ratios (see table 1). The resulting dissolutions were subsequently frozen in a round-bottom flask that contained liquid nitrogen. Afterwards, the

round-bottom flasks were connected to the freeze-dryer for 48 h at a pressure of $3 \cdot 10^{-1}$ mbar and a temperature of -80 ºC to sublime the solvent. The as-obtained precursors were subjected to a single heat treatment at 700 ºC during 4 h. Subsequently, the products were ball-milled for 30 minutes.

Characterization

Structural characterization of the samples was performed by powder X-ray diffraction with a Bruker D8 Advance Vario diffractometer using CuK_{α} radiation. The obtained diffractograms were fitted using the FullProf program [16]. The morphologies of the materials were observed by Transmission Electron Microscopy (TEM) using a FEI TECNAI F30. X-ray photo electron spectra (XPS) were obtained on an SPECS system equipped with a Phoibos 150 1D-DLD analyzer and a monochromatic AlK_{α} (1486.6 eV) source. A Bruker ELEXSYS 500 spectrometer equipped with a super-high-Q resonator ER-4123-SHQ, operating at X band, was used to record the ESR polycrystalline spectra. Magnetic susceptibility measurements (dc) were carried out between 5K and 300K with a Quantum Design SQUID magnetometer.

2032 coin cells were assembled to test the electrochemical performances of the spinel samples. To prepare the electrodes the active materials were mixed with conducting carbon black (Super P, Timcal) and Polyvinylidene Fluoride (PVDF) binder with the weight ratio of 80:10:10 and dispersed in N-methyl-2-pyrrolidone (NMP) to form a slurry. The slurry was then cast onto Al current collectors and dried at 120ºC in a vacuum oven overnight. Electrochemical cells were assembled in an Ar filled glove box with metallic lithium foil as

the counter electrode, Celgard 2400 polypropylene separators and 1 M $LiPF_6$ in 50%-50% ethyl carbonate (EC) and dimethyl carbonate (DMC) as the electrolyte. All the electrochemical measurements were carried out on a Bio-Logic VMP3 potentiostat battery tester at room temperature. Typical electrode loadings were 1.3 mg/cm^2.

The galvanostatic charge/discharge experiments were performed between 3.5 and 4.3V at 0.1C and 1C current rates. 1C was calculated based on full delithiation of spinel samples, $LiMn_{2-x}Si_xO_4 \leftrightarrow Li + Mn_{2-x}Si_xO_4$. In addition, the rate capability of the materials was characterized through the acquisition of a "signature curve" (SC) [17], obtained by a protocol that consists of an initial charge performed at 0.1C followed by a series of successive discharges at different rates, from highest (10C) to lowest (0.1C), with relaxation periods of 5 min and no charging step in between.

Results and discussion

Figure 1 shows the XRD patterns of all $LiMn_{2-x}Si_xO_4$ samples. All of the diffraction peaks could be indexed to the cubic spinel Fd-3m space group. A weak reflection corresponding to a Mn_3O_4 impurity was detected at $2\theta \approx 26^\circ$ in $LiMn_{1.8}Si_{0.2}O_4$, while no impurities were detected for the rest of the samples. The values of the cell parameters and volumes resulting from profile-fitting the patterns are shown in table 1. The value of the cell parameter increased with the Si(IV) content, strongly suggesting that the ion incorporated into the spinel structure. However, the cell volume increase is in apparent contradiction with the fact that, the ionic radius of Si(IV) in an octahedral site [r=0.40Å] is smaller than that of Mn (IV) [r=0.53Å]. Si (IV), can be located either at 8a tetrahedral sites or at 16d

octahedral sites. Nonetheless, the (220) reflection, which arises only from the diffraction of the tetrahedral sites (8a), and which lies at $2\theta \approx 31^{\circ}$, was almost undetectable for all of the patterns [18]. Thus, it can be concluded that the tetrahedral sites are predominantly occupied by very light lithium ions, and that most of the Si (IV) replaces Mn in the octahedral (16d) sites. However, Si (IV) is frequently tetrahedrally coordinated; thus it is not unreasonable to suspect that as the amount of Si (IV) is increased ion-mixing might occur, resulting in compositions $(Li_{1-y}Si_y)_{8a}(Mn_{2-x}Si_{x-y}Li_y)_{16d}O_4$ ($0 \leq x \leq 0.2$). In order to elucidate the effect of Si(IV) on the crystal structure of the spinel, follow-up work with neutron diffraction is required.

Table 1. Synthesis molar ratios and obtained cell parameters volumes for $LiMn_{2-x}Si_xO_4$ ($0 \leq x \leq 0.2$) samples.

Sample	Molar ratio $C_6H_8O_7.H_2O$ $Mn(C_2H_3O_2)_3.$ $Si(CH_3COO)_4$ $LiOH.H_2O$	Cell parameter (Å)	Cell volume (Å^3)
$LiMn_2O_4$	3:2:0:1	8.2361(3)	558.68(1)
$LiMn_{1.95}Si_{0.05}O_4$	3:1.95:0.05:1	8.2363(3)	558.73(1)
$LiMn_{1.9}Si_{0.1}O_4$	3:1.9:0.1:1	8.2394(3)	559.35(1)
$LiMn_{1.8}Si_{0.2}O_4$	3:1.8:0.2:1	8.2414(3)	559.76(1)

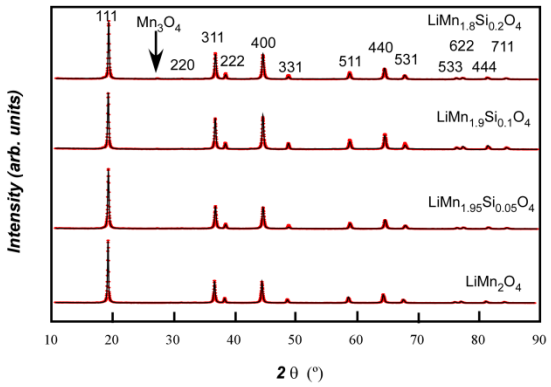

Fig.1 X-ray patterns of $LiMn_{2-x}Si_xO_4$ ($0 \leq x \leq 0.2$) samples.

Figure 2a shows a transmission electron micrograph of $LiMn_{1.95}Si_{0.05}O_4$, which is representative of all materials, as expected from the fact that the synthetic conditions were the same. The freeze-drying method followed by a moderate annealing temperature of 700ºC led to well crystallized grains in all four samples. They were composed of 80 nm average size homogeneous primary particles. The crystals do not present a regular shape and are partially sintered, improving the connection between the particles. Figure 2b shows a high-resolution image of a single crystal of $LiMn_{1.95}Si_{0.05}O_4$, where the (111) crystallographic planes of the spinel structure can be observed.

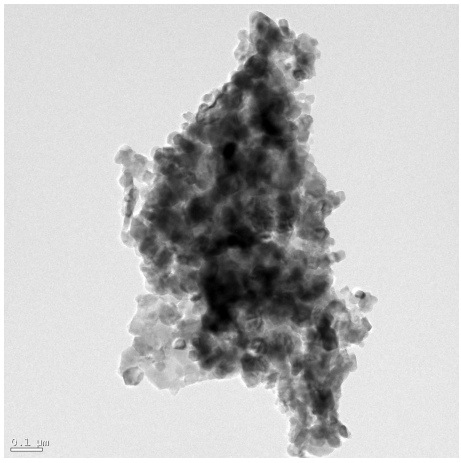

a)

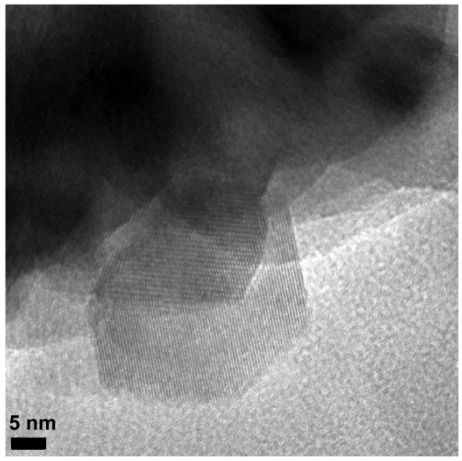

b)

Fig.2 TEM micrographs of the silicon substituted sample $LiMn_{1.95}Si_{0.05}O_4$.

XPS was used to identify the elements in the $LiMn_{2-x}Si_xO_4$ ($0 \leq x \leq 0.2$) compounds and their valence states. High resolution Si 2p and Mn 2p spectra are shown in figures 3 and 4. The binding energy (BE) obtained for Si (2p) is 102 eV. There is no change in BE with Si

contents, but the band area increases as the amount of substituent increases. Indeed, the Si 2p band area for $LiMn_{1.8}Si_{0.2}O_4$ is four times bigger than $LiMn_{1.95}Si_{0.05}O_4$ in good agreement with the nominal increase in Si (IV) amount.

The Mn $2p_{3/2}$ XPS BE of Mn (III) and Mn (IV) ions are at 641.9 and 643.2 eV, respectively [19]. Here, the Mn $2p_{3/2}$ binding energies of the four samples are in this region, which indicates that the Mn valence is in the mixed state. Moreover, the binding energy of Mn $2p_{3/2}$ decreases from 642.6 to 642.4 eV as the Si (IV) content was increased from x=0 to x=0.2, which indicates that the average valence state of Mn ions in the $LiMn_{2-x}Si_xO_4$ (x=0, 0.05, 0.1 and 0.2) compounds decreases as the amount of Mn (IV) is reduced with Si insertion.

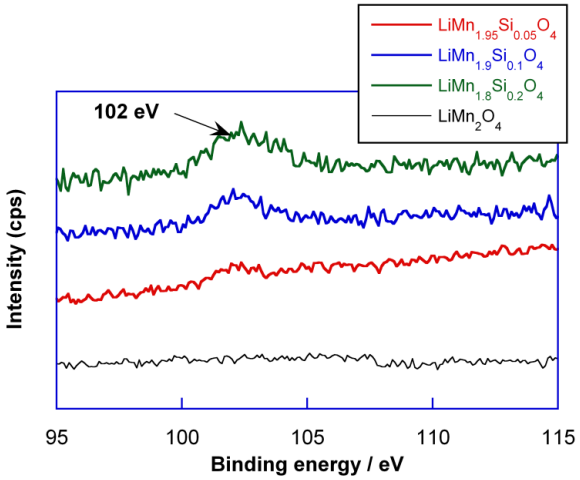

Fig.3 High resolution Si 2p XPS spectra for $LiMn_{2-x}Si_xO_4$ ($0 \leq x \leq 0.2$) samples

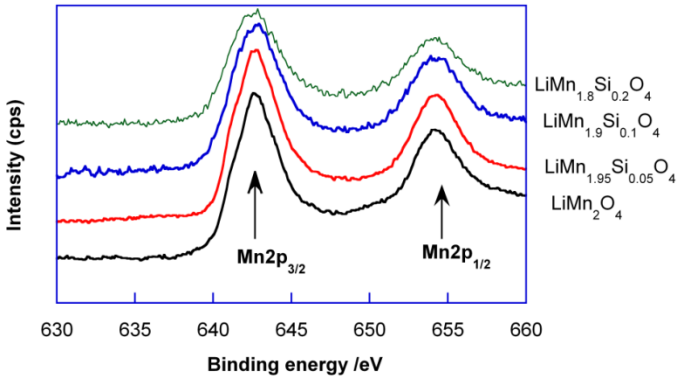

Fig.4 High resolution Mn 2p XPS spectra for $LiMn_{2-x}Si_xO_4$ ($0 \leq x \leq 0.2$) samples.

Figure 5 shows the ESR spectra of the samples, recorded at the X band at room temperature. Similar patterns were observed for all samples: a very broad quasi-isotropic signal centered at a Landé factor g close to 2. This signal is characteristic of exchange coupled Mn(IV)-Mn(III) ions. The g factor does not exhibit any dependency on the chemical composition, but the linewidth of the signal shows a clear dependence on the ratio of Mn(III)/Mn(IV). The peak-to-peak linewidth ΔH_{pp} values are wider than 2500 Oe for all the cases (see inset figure 5). The short spin-lattice relaxation time and large zero-field splitting of Mn (III) hinder the observation of any paramagnetic resonance absorption at X-band corresponding to this ion [20]. Consequently, the magnetic coupling between the Mn (III) and Mn (IV) ions induces a significant broadening of the absorption band of Mn (IV), affected by the short spin-lattice relaxation times of Mn(III). As a result, as the Mn(III)/Mn(IV) ratio becomes larger, the peak to peak linewidth ΔH_{pp} value also increases.

The ΔH_{pp} measured for $LiMn_2O_4$, where the Mn(III)/Mn(IV) ratio is lowest, is also the narrowest one, 2930 Oe. In contrast, the linewidth increases to 3150 Oe and 3532 Oe for $LiMn_{1.95}Si_{0.05}O_4$ (Mn(III)/Mn(IV)= 1.05) and $LiMn_{1.9}Si_{0.1}O_4$ (Mn(III)/Mn(IV)= 1.1). The signal for $LiMn_{1.8}Si_{0.2}O_4$ disappears due to the high proportion of Mn(III) in the total Mn content that this sample exhibits. All in all, the broadening effect is more perceptible as the relative content of Mn(III) is greater. Therefore, this technique supports the existence of an effective substitution of Mn by Si in the spinel framework.

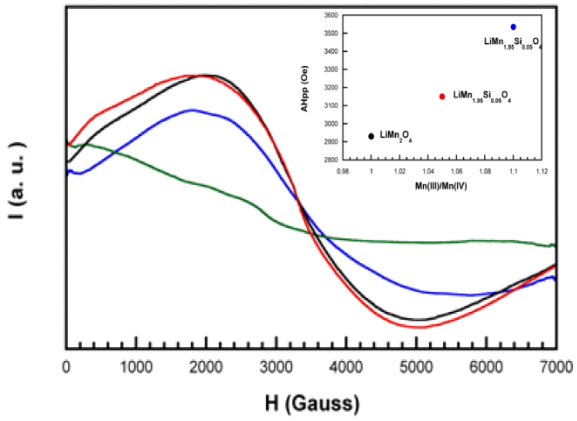

Fig.5 ESR spectra at X band at room temperature for $LiMn_2O_4$ (black), $LiMn_{1.95}Si_{0.05}O_4$ (red), $LiMn_{1.9}Si_{0.1}O_4$ (blue) and $LiMn_{1.8}Si_{0.2}O_4$ (green) samples. Inset: peak-to-peak linewidth (ΔHpp) as a function of the Mn(III)/Mn(IV) rate

Magnetic susceptibility (χ_m) measurements of the samples were carried out in the 5-300 K temperature range at 1 KOe. Figure 6 shows the thermal evolution of χ_m for $LiMn_{2-x}Si_xO_4$, ($0 \leq x \leq 0.2$). The ZFC showed a maximum in χ_m in all cases, which is indicative of

predominantly antiferromagnetic interactions. The temperatures at which the maximum of χ_m is located are shown in table 2. Even if the maximum in χ_m appears at ZFC, FC curves diverge at 45K in all cases, showing the appearance of weak ferromagnetism below that temperature. The anomaly that appears at 43K for $LiMn_{1.8}Si_{0.2}O_4$ can be attributed to a small amount of the Mn_3O_4 ferrimagnetic oxide appearing as an impurity [21]. Figure 7 shows the thermal evolution of $\chi_m T$ of all the samples. $\chi_m T$ exhibits a continuous decay from 300 K, which is again indicative of the existence of strong antiferromagnetic interactions below room temperature. The effective magnetic moments per mol of spinel at 300 K, $\mu_{eff} = \sqrt{8\chi_m T}$, are presented in table 2. The decrease of the μ_{eff} as Si(IV) is increased, agrees with the reduction of the amount of magnetic ions in the sample.

The magnetic sublattice in the spinel structure consists of a network of vertex-sharing Mn tetrahedra known as the pyrochlore network. The antiferromagnets that have this connectivity are frustrated systems because the four magnetic moments of the Mn ions located at the vertexes of a tetrahedron cannot align themselves in such a way as to be simultaneously antiparallel to each other. Thus, the Mn sublattice in the $LiMn_2O_4$ parent spinel satisfies the condition of a magnetically frustrated system [22]. In addition, superexchange 90º $Mn^{III/IV}$-O-$Mn^{III/IV}$ and direct $Mn^{III/IV}$-$Mn^{III/IV}$ interactions are also possible between the nearest Mn neighbors. According to Goodenough-Kanamori rules [23], only 90º Mn^{IV}-O-Mn^{IV} coupling will be ferromagnetic, while all other possibilities will be antiferromagnetic. Thus, a spin-glass-like behavior has been reported for some $LiMn_2O_4$ spinel samples, as a result of the magnetic disorder generated by the frustration and the

existence of different contending magnetic interactions [24,25]. However, other possibilities such as a canted antiferromagnetic ordering of spins, and the coexistence of a long-range ordered state with a significant fraction of spins remaining disordered at low temperatures have been also published [26]. A recent publication of our group that reports on the ac susceptibility measurements of this type of spinels showed the existence of a complex magnetic behavior with the presence of partially ordered magnetic clusters of different sizes (see ref 11).

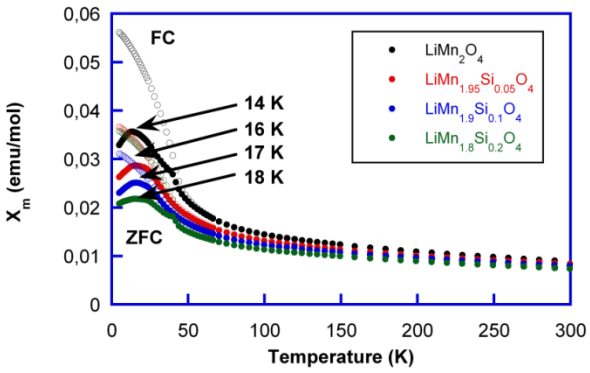

Fig.6 Thermal evolution of molar susceptibility for field cooled (FC) and zero field cooled (ZFC) $LiMn_{2-x}Si_xO_4$ ($0 \leq x \leq 0.2$) samples

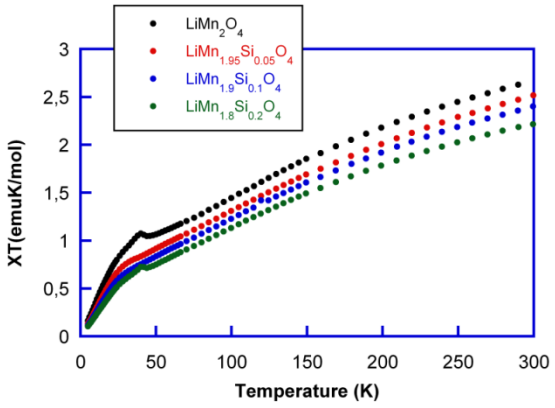

Fig.7 Inverse of the susceptibility for $LiMn_{2-x}Si_xO_4$ ($0 \leq x \leq 0.2$) samples

In the case of the samples in this study, not only does the temperature value of the maximum in χ_m change as Si (IV) is introduced, but also the shape of the ZFC curve. As the Si (IV) amount is increased the maximum of the ZFC curve broadens and becomes less pronounced. This effect can be ascribed to the increase of the effective spin of the magnetic system due to the higher ratio of Mn(III)/Mn(IV) as a result of the Si substitution. Note that Mn(III) is a S=2 ion and Mn(IV) a S= 3/2 ion, so that the S average value increases by decreasing the Mn(IV) amount. Accordingly, for systems with similar magnetic couplings, the temperature of the maximum χ_m increases with S and the peak profile evolves in the same way than that observed for the present samples [27]. However, it is important to note that the insertion of the diamagnetic Si(IV) ion reduces the amount of the magnetic ions in the sample. Therefore, the magnetic coupling between manganese ions is partially hindered when Si (IV) is increased. Moreover, the progressive rising of Mn(III)/Mn(IV) ratio

encourages the competition between the different magnetic exchange pathways, inducing a widening of the range of temperatures for the magnetic transition. The different short-range spin correlations inside several clusters encourage the disorder in the systems. Thus, the nature of the weak ferromagnetic component at low temperatures together with the evolution of the magnetic behavior that has been seen with the insertion of Si(IV) in $LiMn_{2-x}Si_xO_4$, agrees with the progressive increase of the S average value and a higher magnetic disorder in the system.

Table 2 Temperatures of the maximum in χ_m , the effective magnetic moments and specific discharge capacities at C/10 and 1C obtained for $LiMn_{2-x}Si_xO_4$ ($0 \leq x \leq 0.2$) samples

Sample	**Temperature of the maximum in χ_m (K)**	**μ_{eff} per mol of spinel**	**Specific Discharge Capacity C/10 (mAh/g)**	**Specific Discharge Capacity 1C (mAh/g)**
$LiMn_2O_4$	14	4.62	114	99
$LiMn_{1.95}Si_{0.05}O_4$	16	4.48	122	104
$LiMn_{1.9}Si_{0.1}O_4$	17	4.38	87	74
$LiMn_{1.8}Si_{0.2}O_4$	18	4.20	83	69

To evaluate the electrochemical performance lithium half-cells containing the spinels were discharged at a current rate corresponding to C/10 and 1C. Figure 8 shows the first discharge profiles of all samples at C/10 at room temperature. It can be seen that all discharge curves have two voltage plateaus at approximately 4.0 and 4.1 V, which are typical of $LiMn_2O_4$ and its variants. The two voltage plateaus indicate that the extraction (and subsequent re-insertion) of lithium ions from tetrahedral sites occur in two stages. The initial specific discharge capacity of the unsubstituted spinel was 114 mAh/g. The insertion of a small amount of Si(IV) increased this value to 122 mAh/g for $LiMn_{1.95}Si_{0.05}O_4$. However, further increases in substitution lead to actual decreases in this figure of merit; $LiMn_{1.9}Si_{0.1}O_4$ and $LiMn_{1.8}Si_{0.2}O_4$ showed an initial discharge capacity of 87 and 83 mAh/g, respectively. At 1C, the capacity values of all the samples decreased (table 2). The cycling performance is shown in figure 9. After 100 cycles at 1C, the capacity retention for all compounds was high, close to 100%.

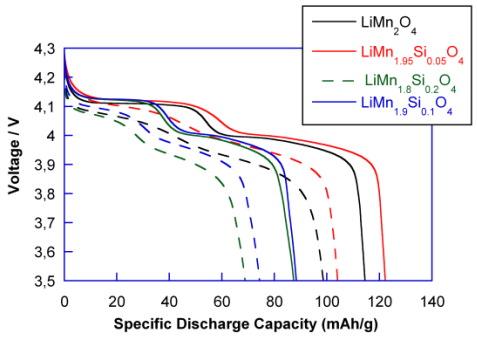

Fig.8 Initial discharge curves at C/10 and 1C for $LiMn_{2-x}Si_xO_4$ ($0 \leq x \leq 0.2$) samples

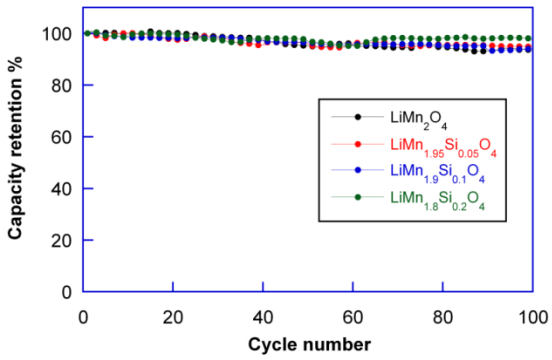

Fig.9 Cycling performance of $LiMn_{2-x}Si_xO_4$ ($0 \leq x \leq 0.2$) samples

The rate capability of the samples was evaluated using signature curves as described in reference 17. Cells were first charged to 4.3 V at 0.1C and discharged to 3.5 V at different rates, starting with the highest one, with five minute rests in between but no charging. The cumulative charge passed at each rate was taken as the capacity values for the given rate. Figure 10, which shows the modified Peukert plot for cells containing the various spinel samples, indicates that the $LiMn_{1.95}Si_{0.05}O_4$ spinel had the best rate performance, giving a specific discharge capacity of 101 mAh/g at 10C. $LiMn_{1.9}Si_{0.1}O_4$ sample also had a good rate capability response as at 10C the capacity retention of the sample was close to the 70% of the initial value. These results clearly show that introducing small amounts of Si (IV) has beneficial effects on the electrochemical properties of $LiMn_2O_4$. Nevertheless, the rate capability deteriorated when the amount of tetravalent substituent was increased further. The capacity retention of $LiMn_{1.8}Si_{0.2}O_4$ sample at 10C was close to zero. This fact could be partially ascribed to the presence of the Mn_3O_4 impurity, as well as to ion mixing due to

the progressive introduction of Si (IV) in the tetrahedral sites.

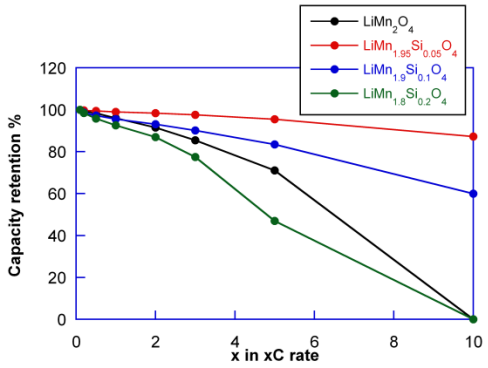

Fig.10 Discharge rate capability for $LiMn_{2-x}Si_xO_4$ ($0 \leq x \leq 0.2$) samples

Conclusions

The freeze-drying method is a useful and easily scalable synthetic procedure to obtain $LiMn_2O_4$ and Si substituted variants. Homogeneous, crystalline and partly sintered samples with intermediate particle sizes were obtained after a short heat treatment at 700 ºC. The presence of bulk particles that consist of aggregated nano-sized particles provides good capacity values even at 10C. The unit cell dimensions as well as the spectroscopic and magnetic properties of the resulting oxides were affected by the introduction of Si(IV). The cationic disorder induced by substitution, together with the in-built magnetic frustration of the spinel structure causes a complex magnetic behaviour in which different short-range interactions are competing. Although the main interactions are antiferromagnetic, the nature of the weak ferromagnetic component at low temperatures indicates the existence of magnetic clusters of many types. The introduction of Si(IV) increases magnetic disorder.

The insertion of high amounts of Si (IV) degrades the electrochemical performance of the spinel, but small amounts of the substituent enhances the electrochemical performance. High capacity retention at 1C was observed for all samples, whereas $LiMn_{1.95}Si_{0.05}O_4$ showed the best rate capability, with a specific capacity of 100 mAh/g at 10C.

Acknowledgments

This work was financially supported by the Ministerio de Ciencia e Innovación (MAT2010-19442) and the Gobierno Vasco/Eusko Jaurlaritza (IT570-13, ETORTEK CICENERGIGUNE10, SAIOTEK S-PE12UN140). A.I. thanks the Gobierno Vasco/Eusko Jaurlaritza for a fellowship. CK, MMD and JC wish to acknowledge financial support by the Assistant Secretary for Energy Efficiency and Renewable Energy, Office of Vehicle Technologies of U. S. Department of Energy, under contract DE-AC02-05CH11231, as part of the Batteries for Advanced Transportation Technologies (BATT) Program.

Notes and references

[a] *Departamento de Química Inorgánica, Universidad del País Vasco UPV/EHU, P.O. Box 644, 48080, Bilbao, Spain.*

[b] *Environmental Energy Technologies Division, Lawrence Berkeley National Laboratory, 1 Cyclotron Rd. MS62R0203, Berkeley, CA 94720-8168, USA*

[c] *CIC energiGUNE, Parque Tecnolóogico de Álava. Albert Einstein 48, 01510 Miñano, Álava, Spain. Tel: +34945 297 108; E-mail: trojo@cicenergigune.com*

[1] M. M. Thackeray, *J. Electrochem. Soc*. , 1995, **142**, 2558.

[2] Y. Xia, and M. Yoshio, *J. Electrochem. Soc*. , 1996, **143**, 825.

[3] Y. Xia, Y. Zhou, and M. Yoshio, *J. Electrochem. Soc*. 144 (1997) 2593-2599.

[4] K. Y. Chung, and K-B. Kim, *Electrochim. Acta* , 2004, **49**, 3327- 3337

[5] S. C. Park, Y. S. Han, Y. S. Kang, P. S. Lee, S. Ahn, H. M. Lee, and J. Y. Lee, *J. Electrochem. Soc*., 2001, **148**, A680-A687.

[6] W. H. Ryu, J. Y. Eom, R. Z. Yin, D. W. Han, W. K. Kim and H. S. Kwon, *J. Chem. Mater*., 2011, **21**, 15337.

[7] R. Thirunakaran, A. Sivashanmugan, S. Gopukumar and R. Rajalakshmi, *J. Power Sources*, 2009, **187**, 565.

[8] P. Poizot, S. Laurelle, S. Grugeon, L. Dupont, and J. M. Tarascon, *Nature*, 2000, **407**, 496-499.

[9] L. Hernan, J. Morales, L. Sanchez, J. Santos, and E. Rodriguez-Castellon, *Solid State Ionics* , 2000, **133**, 179.

[10] C. Sigala, D. Guyomard, A. Verbaere, Y. Piffard and M. Tournoux, *Solid State Ionics*, 1995, **81**, 167.

[11] A. Iturrondobeitia, A. Goñi, V. Palomares, I. Gil de Muro, L. Lezama, and T. Rojo, *J. Power Sources* , 2012, **216**, 482.

[12] C. Liu, F. Li, L. P. Ma and H. M. Cheng, *Adv. Mater*., 2010, **22**, E28.

[13] P. Bruce, B. Scrosati and J. M. Tarascon*, Angew. Chem. Int. Ed.*, 2008, **47**, 2930.

[14] V. Palomares, A. Goñi, I. Gil de Muro, I. de Meatza, M. Bengoechea, I. Cantero and T. Rojo, *J. Electrochem. Soc.*, 2009, **156**, A817.

[15] V. Palomares, A. Goñi, I. Gil de Muro, I. de Meatza, M. Bengoechea, I. Cantero and T. Rojo, *J. Power Sources*, 2007, **171**, 879.

[16] Rodríguez-Carvajal, J.http://valmap.dfis.ull.es/fullprof/index.php

[17] M. Doyle, J. Newman and J. Reimers, *J. Power Sources* , 1994, **52**, 211.

[18] C. Bellito, E. M. Bauer, G. Righini, M. A. Green, W. R. Branford, A. Antonini and M. Pasquali, *J. Phys. Chem. Solids,* 2004, **65**, 29.

[19] K. M. Shaju, G. V. Subba Rao and B. V. R. Chowdari, *Solid State Ionics*, 2002, **69**, 35-45.

[20] D. Capsoni, M. Bini, G. Chiodelli, P. Mustarelli, V. Massarotti, C. B. Azzoni, M. C. Mozzati and L. Linati, *J. Phys. Chem.,* 2002, **106**, 7432-7438.

[21] L. Ortega San Martin, J. P. Chapman, L. Lezama, J. Sanchez Marcos, J. Rodriguez-Fernandez, M. I. Arriortua and T. Rojo, *Eur. J. Inor. Chemistry* , 2006, 1362.

[22] J.E.Greendan, N.P. Raju, A.S. Wills, C. Morin and S.M. Shaw, *Chem. Mater.* , 1998, **10**, 3058.

[23] J.B. Goodenough, Magnetism and the chemical bond, Wiley, New York, 1963.

[24] Y.I. Jang, F.C. Chou and Y.M. Chiang, *Appl. Phys. Lett.* , 1999, **74**, 2504.

[25] V. Kusigerski, D. Markovic, V. Spasojevic, N. Cvjeticanin, M. Mitric, D. Jugovic and D. Uskokovic, *J. Magn. Mater.*, 2008, **320**, 943.

[26] A. S.Wills, N. P.Raju and J. E.Greendan, *Chem. Mater*. , 1999, **11**, 1510.

[27] R. L. Carlin, A. J. Van Duyneyeldt, Magnetic Properties of Transition Metal Compounds, Springer-Verlag, New York, 1977.